


## Article

# Investigation on the Impacts of Three Sea Salt Ions on the Performance of CSA-OPC Binary System

Chuanlin Wang<sup>1,2,\*</sup> , Shupeng Zhou<sup>1</sup>, Qingyou Ou<sup>1</sup> and Yuxuan Zhang<sup>1</sup>

<sup>1</sup> Department of Civil Engineering and Smart Cities, Shantou University, Shantou 515063, China; zsp1700042701@163.com (S.Z.); ou1271513993@outlook.com (Q.O.); 16yxzhang3@alumni.stu.edu.cn (Y.Z.)

<sup>2</sup> Guangdong Engineering Center for Structure Safety and Health Monitoring, Shantou 515063, China

\* Correspondence: clwang@stu.edu.cn

**Abstract:** This study aimed to explore the impact of three corrosive ions— $\text{SO}_4^{2-}$ ,  $\text{Cl}^-$ , and  $\text{Mg}^{2+}$ —on the hydration property of calcium sulphoaluminate (CSA) cement. Cement paste was prepared using three types of sea salt ion solutions with varying concentrations as mixing water. The experimental program encompassed assessments of porosity, compressive/flexural strength, heat of hydration, pH of pore solution, XRD, and SEM analysis. To modulate the hydration environment, Ordinary Portland cement (10%) was incorporated to elevate the pH and enhance the stability of ettringite, thereby facilitating the formation of additional C-S-H gel for the observation of M-S-H and other compounds. Findings revealed that the  $\text{Cl}^-$  accelerated the hydration of CSA, resulting in heightened heat release. However, it also decreased the length-to-diameter ratio of ettringite, leading to cracking in CSA test blocks. The addition of  $\text{SO}_4^{2-}$  resulted in elevated internal alkalinity, prompting alterations in hydration product types and subsequent reduction in CSA strength. Conversely,  $\text{Mg}^{2+}$  was observed to ameliorate the microstructure of CSA test blocks, diminishing porosity and augmenting strength.

**Keywords:** sulphoaluminate cement; sea salt; expansion; heat of hydration; pH; microstructure



**Citation:** Wang, C.; Zhou, S.; Ou, Q.; Zhang, Y. Investigation on the Impacts of Three Sea Salt Ions on the Performance of CSA-OPC Binary System. *Buildings* **2024**, *14*, 1481. <https://doi.org/10.3390/buildings14051481>

Academic Editor: Francisco López-Almansa

Received: 30 April 2024

Revised: 14 May 2024

Accepted: 17 May 2024

Published: 20 May 2024



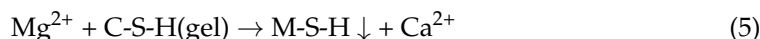
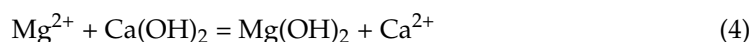
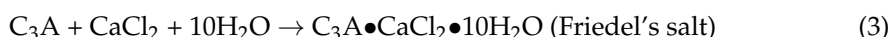
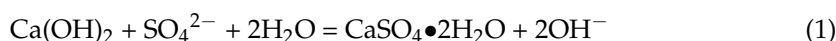
**Copyright:** © 2024 by the authors. Licensee MDPI, Basel, Switzerland. This article is an open access article distributed under the terms and conditions of the Creative Commons Attribution (CC BY) license (<https://creativecommons.org/licenses/by/4.0/>).

## 1. Introduction

Seawater constitutes 97.3% of the Earth's total water storage, with freshwater accounting for merely 2.7%, of which less than 1% is readily usable [1]. Therefore, utilization of seawater to replace freshwater in concrete mixing is becoming a research hotspot in the civil engineering field. In the 1970s, the Chinese Academy of Building Materials developed calcium sulphoaluminate (CSA) cement [2–5], recognized for its principal hydration products, notably ettringite (AFt), AFm, and AH3. Particularly in marine settings, CSA concrete exhibits diminished chloride ion diffusion coefficients and heightened resistance to chloride ions. Moreover, the hydration product AFt within CSA demonstrates limited reactivity with  $\text{SO}_4^{2-}$  and  $\text{Mg}^{2+}$  present in seawater, ensuring the durability of CSA concrete [6]. Consequently, CSA emerges as a promising material for employment in marine engineering. Nonetheless, the extensive presence of ions in seawater poses potential challenges, as these sea salt ions ( $\text{SO}_4^{2-}$ ,  $\text{Cl}^-$ ,  $\text{Mg}^{2+}$ ) profoundly influence CSA hydration by engaging in the hydration process and altering the pH environment of CSA hydration [7–9].

The influence of  $\text{SO}_4^{2-}$  on CSA primarily involves the formation of gypsum, AFt, and salt crystals, as illustrated in Equations (1) and (2) [9–11]. As a constituent of the hydration process,  $\text{SO}_4^{2-}$  can expedite the hydration of CSA clinker ( $\text{C}_4\text{A}_3\text{S}$ ), leading to the generation of ettringite and contributing to strength development. However, excessive  $\text{SO}_4^{2-}$  levels may compromise structural integrity due to inadequate resistance to ettringite expansion stress, resulting in strength reduction [12,13]. Despite extensive research, there is still no definitive concentration standard to ascertain the beneficial effects of  $\text{SO}_4^{2-}$  on CSA. The influence of  $\text{Cl}^-$  on CSA primarily manifests through its involvement in early hydration. It can directly react with CSA to produce Friedel's salt, as demonstrated in

Equation (3) [14–16]. However, existing research lacks consensus regarding the characteristics of Friedel’s salt. According to Kim’s findings [17], Friedel’s salt can densify the interior of CSA by filling pores, thereby enhancing strength development. Conversely, some studies suggest that Friedel’s salt formation depletes the aluminum phase, leading to decreased ettringite content and CSA strength [18]. The influence of  $Mg^{2+}$  on CSA mainly involves its substitution for  $Ca^{2+}$ . On one hand,  $Mg^{2+}$  reacts with calcium hydroxide to produce less soluble brucite ( $Mg(OH)_2$ ), which coats the cement surface and retards early hydration [19]. On the other hand,  $Mg^{2+}$  replaces  $Ca^{2+}$  in C-S-H gel, forming anhydrous rigid M-S-H gel and reducing bond strength, as depicted in Equations (4) and (5) [20]. However, certain studies [21–24] suggest that  $Mg^{2+}$  positively impacts CSA compressive strength by accelerating cement hydration in later stages and promoting the formation of AFt and  $Ca(OH)_2$ .



Moreover, coupling effects arise when multiple sea salt ions coexist [19,25]. To mitigate the coupling effect among  $SO_4^{2-}$ ,  $Cl^-$ , and  $Mg^{2+}$  ions, solutions of NaCl,  $NaSO_4$ , and  $Mg(CH_3COO)_2$  were utilized as mixing water to examine their individual and collective influences on CSA hydration. Since ettringite cannot stably exist in an environment with a pH below 10.7 [26], and CSA cement contains low levels of  $C_2S$  and  $C_3S$ , which hinders observation of its hydration products like the C(M)-S-H gel, this study incorporated 10% ordinary Portland cement (OPC) to enhance the alkalinity and facilitate the formation of gel-like hydration products such as C-S-H for improved observation [27]. At present, research on the interaction between the main corrosive ions in the marine environment and the internal microenvironment of cement-based materials mainly focuses on single ions, and there has been no study on the influence of sea salt ions on the CSA-OPC binary system. Therefore, this study provides valuable insights for research on seawater-mixed concrete through a comprehensive investigation employing various analytical techniques including hydration heat analysis, mechanical and chemical property tests, XRD, and SEM, and it studies the impact of  $SO_4^{2-}$ ,  $Cl^-$ , and  $Mg^{2+}$  on the hydration process of CSA-OPC.

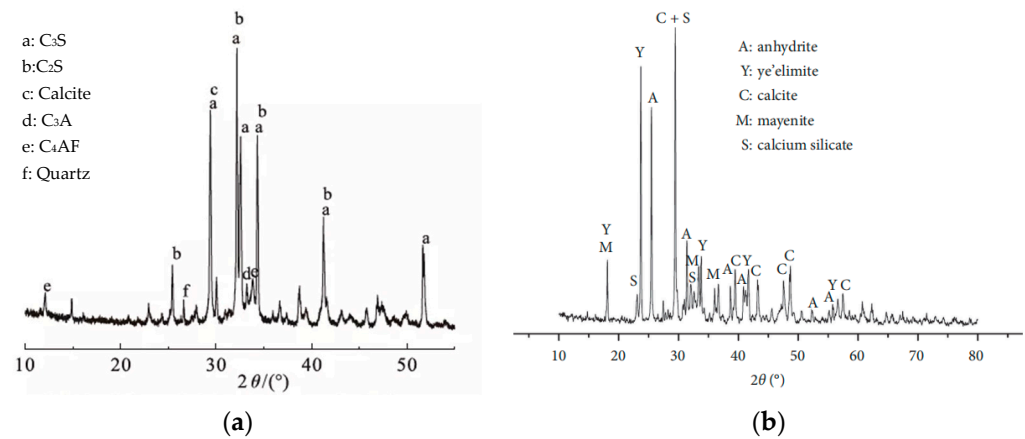
## 2. Experimental Materials and Methods

### 2.1. Raw Materials

The experimental study utilized ordinary Portland cement (OPC), specifically P.O 42.5 from China Resources Corporation, and R. SAC 42.5 rapid hardening sulphoaluminate cement from Guangxi Yunyan Co., Ltd. (Guilin, China). Their chemical compositions are presented in Table 1, while the XRD patterns of OPC and CSA clinkers are depicted in Figure 1. River sand ranging in diameter from 0.15 to 1.18 mm was employed. The mixing water comprised solutions of NaCl,  $NaSO_4$ ,  $Mg(CH_3COO)_2$ , and freshwater. Initial solution concentrations were manufactured based on the predominant salt ion levels in seawater near Shantou Bay (refer to Table 2), with solutions also prepared at 2 and 3 times seawater concentration. Detailed mixing proportions for each solution are outlined in Table 3, with deionized water serving as freshwater. After preliminary experiments, the optimal mixing ratio of CSA-OPC composite system was determined to be 9:1.

**Table 1.** Chemical composition of cement (wt%).

Name	CaO	SiO <sub>2</sub>	Al <sub>2</sub> O <sub>3</sub>	Fe <sub>2</sub> O <sub>3</sub>	SO <sub>3</sub>	MgO	TiO <sub>2</sub>	K <sub>2</sub> O	Na <sub>2</sub> O
OPC	57.80	21.83	3.59	6.30	0.35	2.61		0.84	0.23
CSA	45.30	7.23	18.60	4.30	12.50	1.35	0.87		

**Figure 1.** XRD pattern of binding materials:(a) OPC clinkers; (b) CSA clinkers.**Table 2.** Main chemical composition of seawater (g/L).

Ion	Cl <sup>-</sup>	SO <sub>4</sub> <sup>2-</sup>	Na <sup>+</sup>	Mg <sup>2+</sup>	Ca <sup>2+</sup>
Concentration	16.50~18.50	2.00~2.60	9.50~10.50	0.95~1.40	0.28~0.38

**Table 3.** Different multiples of simulated solution (g/L).

Sample	NaCl	Na <sub>2</sub> SO <sub>4</sub>	Mg(CH <sub>3</sub> COO) <sub>2</sub>
Control			
CL1.0	31.89		
CL2.0	63.78		
CL3.0	95.67		
SO1.0		3.36	
SO2.0		6.72	
SO3.0		10.08	
MG1.0			4.40
MG2.0			8.80
MG3.0			13.20

## 2.2. Preparation Specimens

Researchers noted that substituting 10% of CSA with OPC elevated the pH and marginally enhanced the mechanical strength of the CSA matrix. Consequently, the binding materials consisted of 90% CSA and 10% OPC. A water–cement ratio of 0.5 and sand–cement ratio of 0.5 were maintained. The CSA clinker, OPC clinker, and river sand were mixed and stirred for 2 min before adding the mixing water. The mixture underwent rapid stirring for 1 min followed by slow stirring for 1 min. The resulting CSA-OPC mortar paste was cast into molds with dimensions of 40 mm × 40 mm × 160 mm and cured in a standard curing box for 6 h before demoulding. Additionally, CSA-OPC slurry without sand was prepared. Specimens were subsequently placed in a 20 °C steam curing box until reaching standard age.

## 2.3. Experimental Methods

### 2.3.1. Flexural/Compressive Strength

In accordance with the specifications outlined in the “Test Method of Cement Mortar Strength (ISO Method)” (GB/T 17671-1999) [28], the determination of flexural and compressive

sive strength utilized three prismatic specimens measuring 40 mm × 40 mm × 160 mm per group. The flexural test was conducted at a loading speed of 0.05 kN/s. Subsequently, the remaining halves of the prismatic specimens were employed for the compressive strength test, conducted at a loading speed of 2.4 kN/s, with each group containing six specimens.

### 2.3.2. X-ray Diffraction Analysis

Samples were crushed after reaching standard curing age, and the internal fragments were ground into powder using an agate mortar. The resultant powder was then sealed in a container, and anhydrous ethanol was added to halt hydration. Following this, the powder was dried for 24 h in an oven set at  $(40 \pm 1)$  °C. X-ray diffraction analysis was performed using a Bruker X-ray diffractometer equipped with Cu-K $\alpha$  radiation. The scanning range spanned from 5 to 70°, with a scanning speed of 5°/min.

### 2.3.3. Scanning Electron Microscopy

After the standard curing period, samples of CSA-OPC slurry were crushed, and flat fragments ranging from 2 to 5 mm were selected. These fragments were then placed in a sealed container, where anhydrous ethanol was added to prevent hydration. Subsequently, the fragments were dried for 24 h in an oven set at  $(40 \pm 1)$  °C. Following drying, the fragments were sequentially affixed to a conductive platform and subjected to sputtering treatment in a vacuum device. Then the sputtered samples were observed and imaged using the Gemini300 field emission scanning electron microscope manufactured by Zeiss, with appropriate magnification and positioning selected for observation and photography.

### 2.3.4. Hydration Heat

The hydration heat of CSA-OPC matrix composites was assessed using a TAM Air three-channel calorimeter. Continuous measurements of the heat release rate ( $dQ/dt$ ) and total heat release ( $Q$ ) during the hydration of CSA were recorded over a 24 h period.

### 2.3.5. Apparent Porosity

The apparent porosity of CSA-OPC was determined in accordance with ASTM-C20 standards [29]. As Aft could decompose at high temperatures, each set of three specimens was dried in an oven at 65 °C until reaching a constant weight after curing to standard age, with the dry mass ( $D$ ) subsequently measured. The dried test block was then placed in a vacuum water retention machine to saturate its pores with water. Following saturation, the test block was removed from the machine, and both the saturated mass ( $W$ ) and hanging mass ( $S$ ) were measured. The average value was considered as the result.

### 2.3.6. The pH Value of the Pore Solution

Specimens were ground and sieved using a 0.63 mm sieve. The resulting powder was immersed in distilled water at a water-to-solid ratio of 10:1. The container was sealed with a stopper, vigorously shaken for 2 min, and allowed to stand for 24 h. Subsequently, three portions of 20 mL each of the filtrate were extracted, and their pH values were measured using an acidity meter (pHS-3C). The average value of three samples was considered as the result.

The manufacturing process and the aforementioned experiments are illustrated in Figure 2.



Figure 2. The manufacturing process and experimental method of CSA.

### 3. Results and Analysis

#### 3.1. The Effect of $Cl^-$

##### 3.1.1. The Failure Morphology

Figure 3 displays the failure morphology of specimens cured for 1 d in  $Cl^-$  solutions of varying concentrations. The figure illustrates that all specimens exhibited cracking under different  $Cl^-$  concentrations, indicating noticeable expansion. As the  $Cl^-$  concentration increased, both the crack width and the quantity of cracks in the CSA-OPC specimens increased significantly. At three times the original  $Cl^-$  concentration, specimens exhibited clear signs of splitting and disintegration. The cracks in the matrix are typically attributed to the combined effects of tensile stress from the hydration reaction and thermal stress from hydration heat [4,30]. Therefore, it can be inferred that the addition of  $Cl^-$  accelerated the hydration of the CSA-OPC system, leading to excessive hydration heat and ultimately causing pronounced cracking. As the hydration reactions progress, a significant amount of heat is rapidly released in cement hydration reactions (as indicated in Equation (3)) [31], which can be inferred from the results of the hydration heat reactions.



Figure 3. Appearance of CSA mixed with  $Cl^-$  solution: (a) CL1.0; (b) CL2.0; (c) CL3.0.

##### 3.1.2. Hydration Heat Analysis

Figure 4 illustrates the results of the hydration heat test conducted on CSA-OPC over a 24 h period. The addition of  $Cl^-$  significantly accelerated the hydration of the CSA-OPC system during its induction period, advancing both the induction and decline periods by approximately 2 and 5 h, respectively. Furthermore, a direct relationship was observed between the concentration of  $Cl^-$  solution and the intensity of hydration heat, indicating a pronounced acceleration effect. This phenomenon suggests that  $Cl^-$  promotes the early formation of AFt during CSA-OPC hydration, thereby substantially



shortening the induction period and accelerating the transition into the decline period. The rapid and vigorous hydration reactions led to the rapid release of a large amount of heat, causing a sharp increase in the internal temperature of the CSA, which dissipated slowly. Consequently, significant internal stress developed within the CSA, resulting in deformation and cracking (see Figure 3).

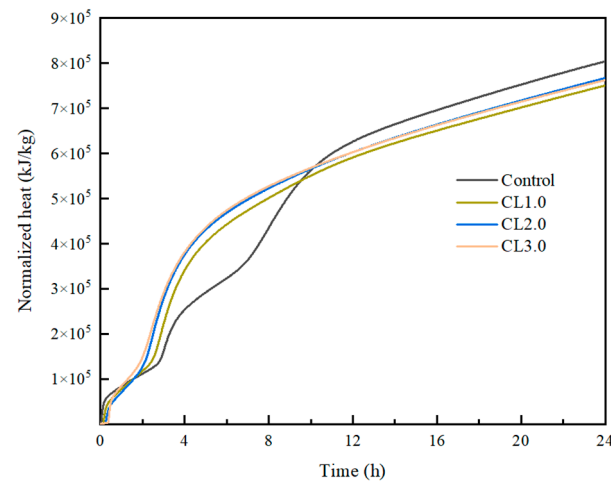


**Figure 4.** Hydration heat of CSA-OPC system mixed with  $\text{Cl}^-$  solution.

### 3.1.3. Hydration Products and Microstructure Analysis

Figure 5 presents the XRD spectrum of CSA-OPC hydration at 3 days. The diffraction peak of CSA-OPC reactants  $\text{C}_4\text{A}_3\text{S}$ ,  $\text{C}_2\text{S}$ , and  $\text{C}_3\text{S}$  in various  $\text{Cl}^-$  concentration groups was lower than that in the freshwater group within the range of  $30^\circ$ . At  $2\theta = 23.5^\circ$ , the diffraction peak of ettringite increased with the increase in  $\text{Cl}^-$  concentration. When  $2\theta$  ranged between  $35.5^\circ$  and  $41.3^\circ$ , although the diffraction peak of ettringite was smaller than that in the freshwater group, it still exhibited an increasing trend with the increase in concentration. Additionally, with the addition of  $\text{Cl}^-$ , the diffraction peak of Friedel's salt appeared at  $2\theta = 16.2^\circ$ , which weakened with the increase in  $\text{Cl}^-$  concentration. This phenomenon suggests that  $\text{Cl}^-$  accelerates the hydration of CSA clinker, and its accelerating effect would increase with the increase in  $\text{Cl}^-$  concentration, consistent with the results of the hydration heat experiment in Section 3.1.2.

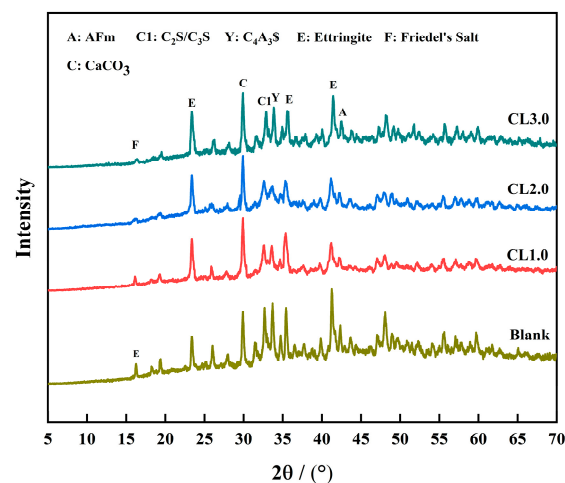


**Figure 5.** XRD pattern of the CSA-OPC slurry.

Figure 6 displays the SEM microstructure figures and EDS spectra of CSA-OPC hydration at 3 days. It is evident from the figures that  $\text{Cl}^-$  significantly impacts the microstructure.

The microstructure of needle-shaped ettringite is connected and intersected in the freshwater group (Figure 6a) and CL1.0 group (Figure 6b), with a clear skeleton, while ettringite appeared in short columnar form in the CL2.0 group (Figure 6c). In the CL3.0 group (Figure 6d), the vast majority of ettringite has transformed into a block shape and is covered by gel-like products. Although the EDS analysis (Figure 6e) indicates that the main composite is ettringite, there is still some amount of Friedel's salt in the products. This suggests that  $\text{Cl}^-$  could alter the morphology of early hydration product (ettringite) in the CSA-OPC system. Ettringite becomes shorter and thicker with the increase in  $\text{Cl}^-$  concentration, which cannot form a strong and intertwined skeleton to provide strength for the matrix. According to Nicolas's research [32,33], the lower the length–diameter ratio of ettringite crystal after nucleation, the greater the expansion stress produced. Additionally, there are wide spaces between needle-shaped ettringite to provide conditions for the crystallization of various substances. Excessive growth stress would occur when ettringite crystals nucleate in small gaps among short and coarse ettringites, which leads to expansive cracks [34–36]. Considering the cracking phenomenon of specimens in Figure 3, it can be inferred that besides accelerating hydration to increase hydration heat,  $\text{Cl}^-$  also alters ettringite morphology, making it shorter and thicker, which produces excessive expansion stress due to lower length–diameter ratio, and then leads to macroscopic cracks.

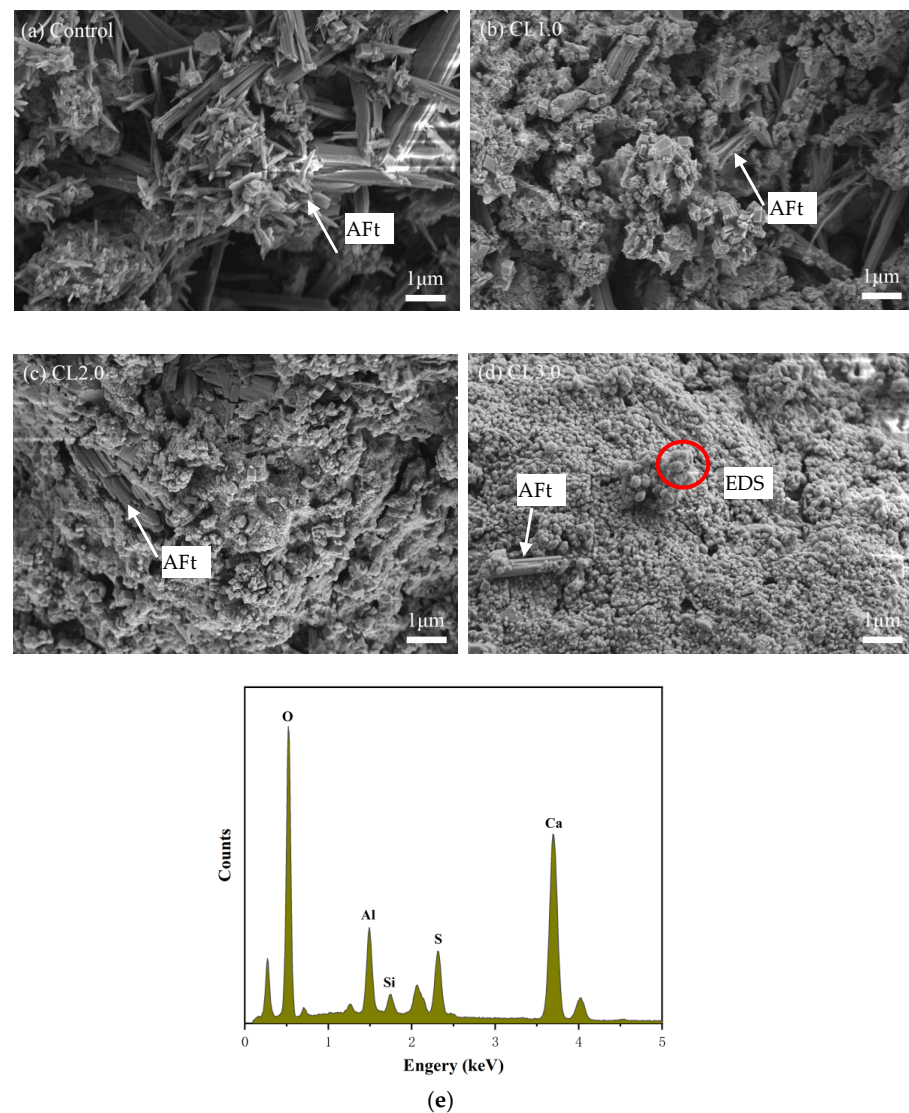


**Figure 6.** SEM images of the 3 d hydration products of CSA mixed with  $\text{Cl}^-$  solution: (a) control; (b) Cl 1.0; (c) Cl 2.0; (d) Cl 3.0; (e) EDS pattern of ettringite.

### 3.2. The Effect of $\text{SO}_4^{2-}/\text{Mg}^{2+}$

#### 3.2.1. The Apparent Porosity

Figure 7 displays the apparent porosity test results of CSA-OPC specimens blended with varying concentrations of  $\text{NaSO}_4$  solution and  $\text{Mg}(\text{CH}_3\text{COO})_2$  solution. The data indicate that the addition of  $\text{SO}_4^{2-}$  led to an increase in the apparent porosity of CSA-OPC, reaching a maximum of approximately 15.4%. Conversely, the incorporation of  $\text{Mg}^{2+}$  resulted in a reduction in apparent porosity, with a maximum decrease of around 12.7%. Furthermore, the porosity of CSA-OPC exhibited an upward trend with increasing  $\text{SO}_4^{2-}$  concentration and decreased as the  $\text{Mg}^{2+}$  concentration rose. These findings suggest that  $\text{SO}_4^{2-}$  contributes to a decrease in the compactness of the CSA-OPC matrix, while  $\text{Mg}^{2+}$  serves to diminish internal pores within the matrix, thereby enhancing its compactness.

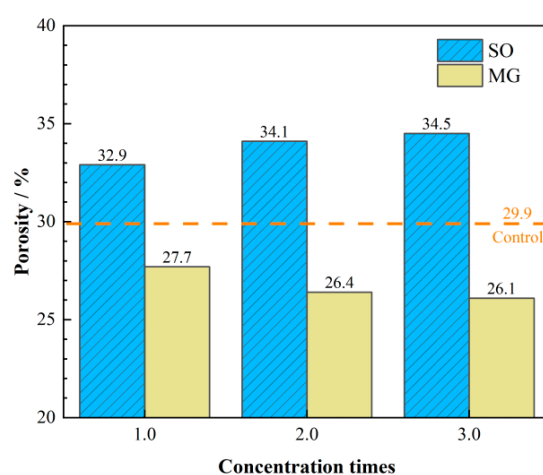


Figure 7. The apparent porosity of CSA-OPC.

The expansive behavior of CSA-OPC systems is predominantly influenced by the formation of ettringite, including factors such as the rate of formation, crystal shape, and crystal size. The addition of a higher quantity of calcium sulfate facilitates the formation of increased ettringite during the hydration process [37]. For this reason, the matrix density decreases with higher sulfate turnover content. Weerdt and Justnes [10] noted that in seawater, as the concentration of  $\text{Mg}^{2+}$  reaches a certain level,  $\text{Mg}^{2+}$  may replace  $\text{Ca}^{2+}$ , potentially leading to the formation of M-S-H. As hydration progresses, more hydration products containing chemically bound water are generated, depleting the free water in seawater and simultaneously increasing the  $\text{Mg}^{2+}$  concentration. This phenomenon further facilitates the substitution of  $\text{Mg}^{2+}$  for  $\text{Ca}^{2+}$  [8]. Consequently, as the magnesium ion content rises, the ettringite content in the matrix diminishes, leading to an increase in the compactness of the cement.

#### 3.2.2. The Flexural/Compressive Strength

The flexural and compressive strength of CSA-OPC specimens mixed with varying concentrations of  $\text{SO}_4^{2-}$  and  $\text{Mg}^{2+}$  solutions are presented in Figure 8. As depicted in Figure 8a,b, except for the SO3.0 group cured at 7 days, the flexural strength of the SO groups at each age was lower than that of the freshwater group. Similarly, the compressive strength, except for the SO2.0 group cured at 7 days and the SO1.0 group cured at 28 days, was lower than that of the freshwater group. However, there was no clear pattern in the strength change of the specimens with increasing  $\text{SO}_4^{2-}$  concentration, suggesting that the inclusion of  $\text{SO}_4^{2-}$  may adversely affect the mechanical properties of the specimens to some extent. According to Equation (1), the introduction of  $\text{SO}_4^{2-}$  should theoretically accelerate hydration to produce more AFt, thereby enhancing strength performance [38]. However, the observed outcome contradicts this expectation, and the rationale behind this discrepancy is elucidated in Section 3.2.3.



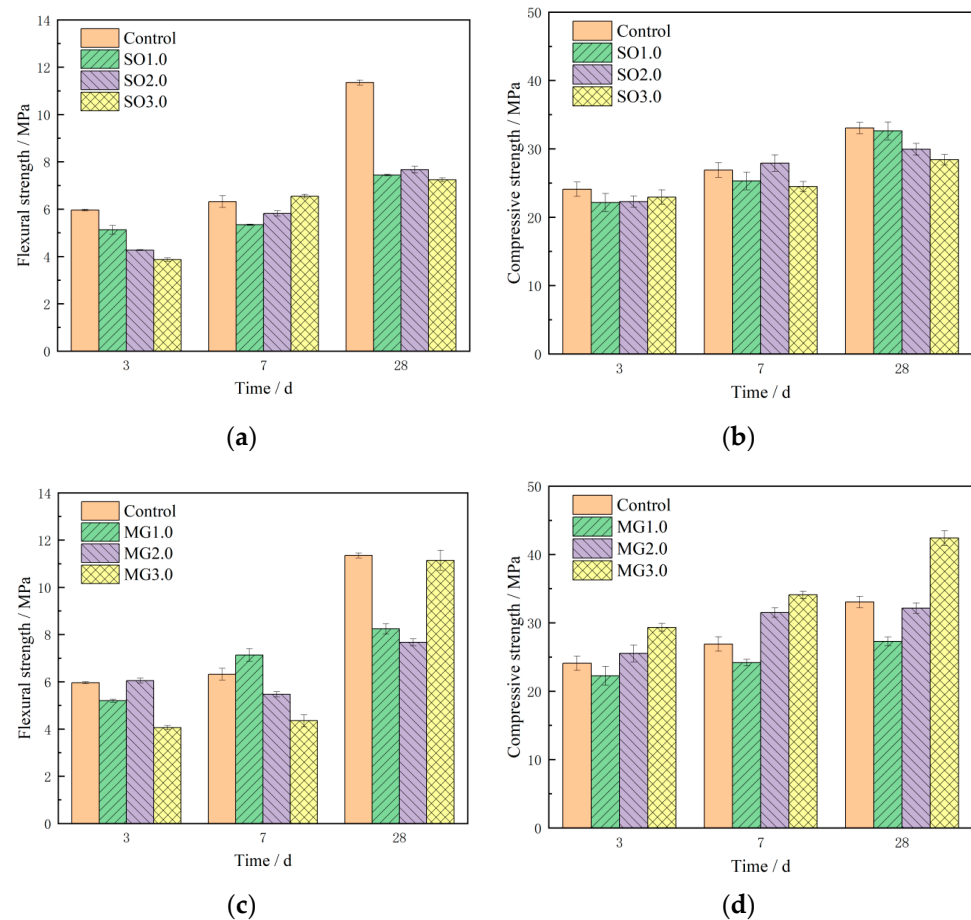


**Figure 8.** Flexural and compressive strength of the CSA-OPC: (a) flexural strength of SO group; (b) compressive strength of SO group; (c) flexural strength of MG group; (d) compressive strength of MG group.

As shown in Figure 8c, with the exception of the 3 d cured MG2.0 group and the 7 d cured MG1.0 group, the flexural strength of specimens in the MG groups was consistently lower than that of the freshwater group across all ages. Notably, there was no discernible pattern between strength and the concentration of  $Mg^{2+}$  solution. In contrast, Figure 8d illustrates that the compressive strength of specimens across all ages surpassed that of the freshwater group, except for the MG1.0 group, and exhibited an increasing trend with higher  $Mg^{2+}$  concentrations. This trend suggests that lower  $Mg^{2+}$  concentrations may compromise the compressive and flexural strength of CSA, while higher concentrations of  $Mg^{2+}$  are conducive to enhancing CSA strength. This phenomenon is attributed to the reaction of  $Mg^{2+}$  with CSA clinker to produce  $Mg(OH)_2$ , which does not directly contribute to strength. However, the addition of a certain amount of OPC to CSA raises the internal pH of CSA, leading to increased  $Mg(OH)_2$  production but decreased CSA strength. Furthermore, the incorporation of OPC into the CSA matrix composites results in a greater presence of C-S-H gel in the hydration products compared to pure CSA paste. With escalating  $Mg^{2+}$  concentrations, excess  $Mg^{2+}$  can react with hydrated C-S-H/C-A-S-H to form magnesium and aluminum phases that fill internal pores within the specimen, thereby enhancing specimen density and strength. This aligns with the observed reduction in porosity in the MG groups as detailed in Section 3.2.1.

### 3.2.3. XRD Analysis and pH of Pore Solution

Figure 9 illustrates the XRD patterns of CSA-OPC systems mixed with  $SO_4^{2-}$  and  $Mg^{2+}$  solutions and cured for 3 days. In Figure 9a, notable alterations in the XRD patterns of CSA-OPC occurred after introducing  $SO_4^{2-}$ . With increasing  $SO_4^{2-}$  concentration,

the diffraction peaks of AFt decreased, accompanied by a drop in diffraction intensity. Simultaneously, the diffraction peak of the CSA clinker vanished, replaced by a CxASHn type. Additionally, the total intensity of diffraction peaks decreased with rising  $\text{SO}_4^{2-}$  concentration, indicating that  $\text{SO}_4^{2-}$  addition did not promote CSA hydration to generate AFt but rather reduced crystal content in the CSA-OPC paste, increasing the gel-like product amount. Figure 10 presents the pH test results of pore solutions extracted from SO/MG groups. It reveals that the pH value of the pore solution in SO groups exceeded 13.2, at least 16.8% higher than that in the freshwater group. Padilla [39] noted that when the  $\text{OH}^-$  concentration in the mixing solution reached 4 mol/L, no calcium aluminate hydrate was observed at any curing age. Guo et al. [40] demonstrated that increasing pH improves continuous connected pores, increasing porosity, consistent with the increased porosity observed in Figure 7 due to  $\text{SO}_4^{2-}$  addition. Ben et al. [41–44] found that high alkalinity in the  $\text{C}_4\text{A}_3\text{S}$  and  $\text{C}_2\text{S}$  hydration environment destabilizes calcium aluminate hydrate, obstructing conventional hydration paths and leading to irregularly shaped AFm and AH3 and siliceous garnet formation instead of calcium aluminate hydrate [45], as depicted in Equations (6)–(8). Lei et al. [46,47] discovered that the decalcification process of cement paste can be delineated into two distinct phases. Initially, in the first stage, there is dissolution of  $\text{Ca}(\text{OH})_2$  within the cement paste. Nearly complete removal of  $\text{Ca}(\text{OH})_2$  takes place, along with partial decalcification of C-S-H. Subsequently, in the second stage, as the C/S ratio of the cement paste diminishes, additional decalcification of C-S-H occurs, consequently influencing the pore structure. Therefore,  $\text{SO}_4^{2-}$  addition elevates the pH of the CSA hydration environment, shifting hydration equilibrium towards Equations (6)–(8), consequently reducing calcium aluminate hydrate content in CSA-OPC and weakening SO group strength.

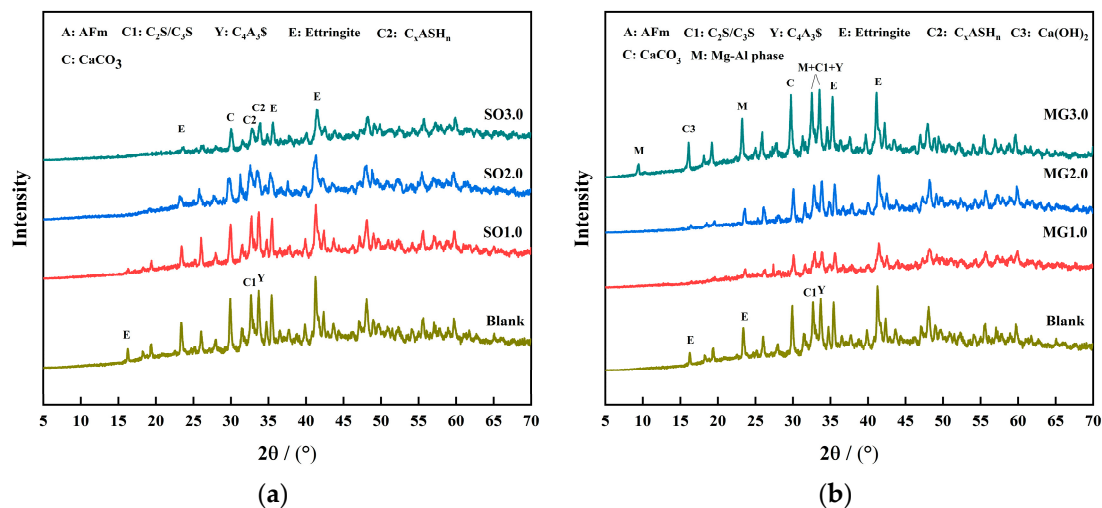
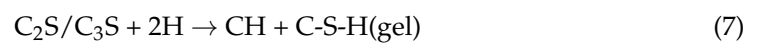
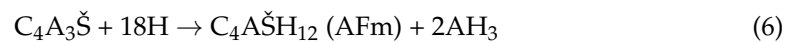
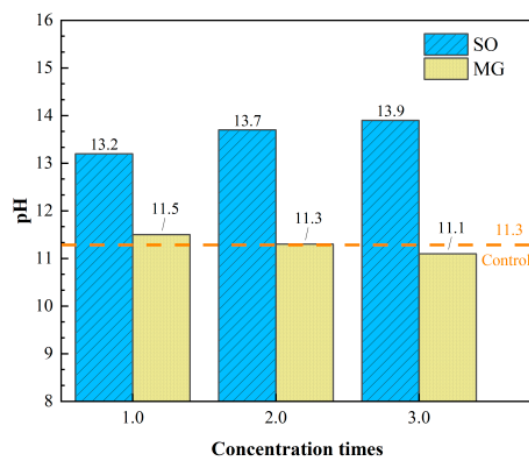


Figure 9. XRD pattern of the 3 d CSA-OPC: (a) SO; (b) MG.



**Figure 10.** pH value of the CSA-OPC.

In Figure 9b, the intensity of the MG group increased with rising  $Mg^{2+}$  concentration. Compared with the freshwater group, diffraction peak intensities of MG1.0/2.0 groups decreased, while that of MG3.0 increased. Numerous magnesium–aluminum substances appeared at  $2\theta = 9.6^\circ$ ,  $23.2^\circ$ , and  $30^\circ < 2\theta < 36^\circ$ , intensifying with higher  $Mg^{2+}$  concentration. At  $2\theta = 16.2^\circ$ , a distinct  $Ca(OH)_2$  peak emerged in the MG3.0 group. When  $Mg^{2+}$  concentration reached 3.0, the calcium aluminate peak intensified. Figure 10 indicates minimal pH impact from  $Mg^{2+}$  addition. Due to the elevated pH of the pore solution in mortar mixtures,  $MgCl_2$  in seawater also reacts with the hydration products of CH to form brucite. As indicated by the equation, the decalcification reaction occurs in C-S-H, where Mg further reacts with decalcified C-S-H to form M-S-H (as depicted in Equations (4) and (5)). These phenomena suggest that adding a small amount of  $Mg^{2+}$  reduces product quantity in the CSA-OPC paste, explaining the strength variation in the MG groups detailed in Section 3.2.2.

### 3.2.4. SEM/EDS Analysis

Figure 11 illustrates the microstructural analysis using SEM and the composition of hydration products using EDS of specimens mixed with freshwater, SO3.0, and MG3.0. In Figure 11a, the hydration products of CSA-OPC in the freshwater group were characterized by the prevalence of elongated, clustered calcium aluminate covered by cementitious material, resulting in a compact structure. Conversely, the SO3.0 group (Figure 11c) displayed a less cohesive structure with less visible ettringite present in short, disconnected columns, failing to form a skeleton structure. Additionally, the quantity of  $C_xASH_n$  (Figure 11d) in the SO3.0 group notably exceeded that in the freshwater group, with segregated cementitious material on the microstructure surface without interconnection. These observations suggest that the addition of  $SO_4^{2-}$  altered the type and morphology of hydration products in the CSA-OPC system. The increased presence of  $C_xASH_n$  indicates a shift in CSA-OPC hydration towards Equation (8) in the XRD analysis, while the stubby shape of ettringite aligns with previous descriptions of ettringite morphology under high alkalinity conditions. These findings also explain the observed increase in porosity and decrease in strength in the SO groups.

Additionally, as depicted in Figure 11b, the MG3.0 group exhibited longer and wider ettringite formations compared to the freshwater group, with a more intact skeleton structure and increased presence of cementitious material filling the gaps within the skeleton. These observations indicate that the substantial addition of  $Mg^{2+}$  enhanced the microstructure of CSA by facilitating ettringite growth and promoting the generation of additional cementitious material, providing a rationale for the strength enhancement observed in the MG groups as discussed in the preceding section.

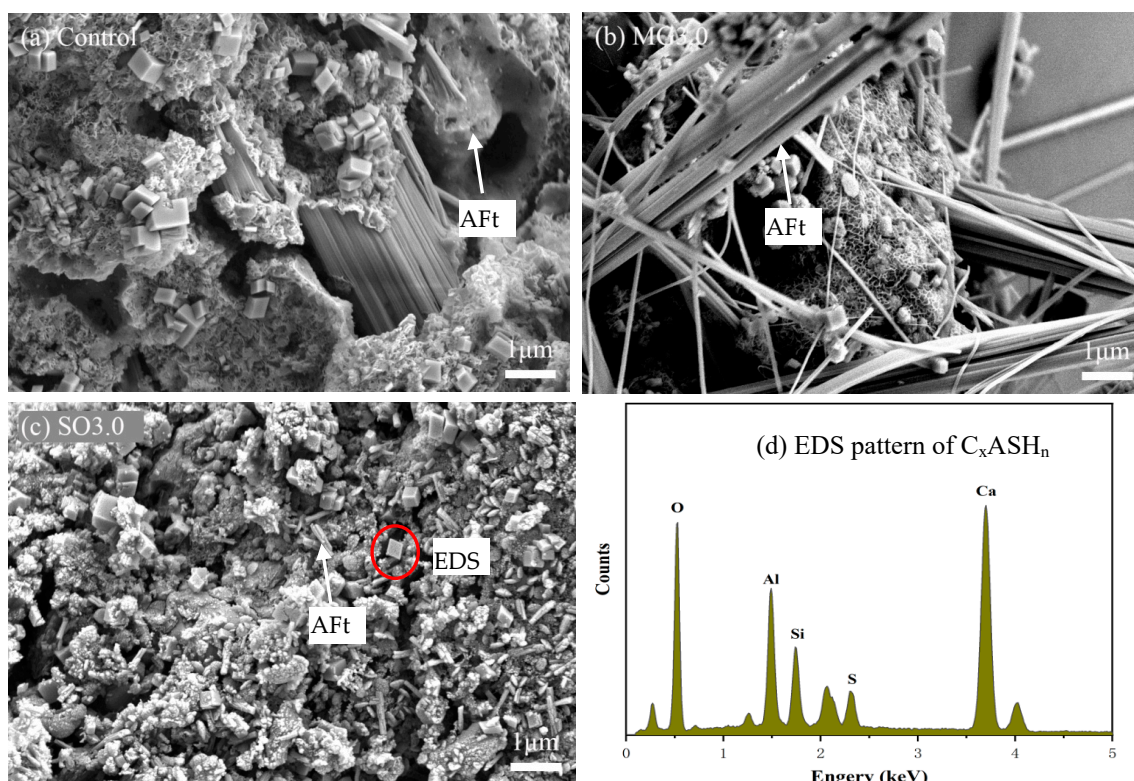


Figure 11. SEM/EDS pattern of 3 d CSA: (a) control; (b) MG 3.0; (c) SO 3.0; (d) EDS and  $C_xASH_n$ .

#### 4. Conclusions

In this investigation, solutions with varying concentrations were established to assess the impact of three sea salt ions ( $SO_4^{2-}$ ,  $Cl^-$ , and  $Mg^{2+}$ ) on the hydration process of a CSA-OPC binary system (90% CSA-10% OPC). The study outcomes are summarized as follows:

(1) Chloride ions ( $Cl^-$ ) induce noticeable expansion and cracking within the CSA-OPC matrix, with wider cracks appearing at higher concentrations. Additionally,  $Cl^-$  accelerates cement hydration, advancing the induction period by approximately 5 h and increasing the heat of hydration within the initial 10 h. Furthermore,  $Cl^-$  alters the microscopic morphology of ettringite in the hydration products, resulting in a reduced length–diameter ratio and enhanced expansion characteristics of ettringite.

(2) The introduction of sulfate ions ( $SO_4^{2-}$ ) leads to a decline in CSA strength, with higher concentrations correlating with lower strength.  $SO_4^{2-}$  also induces changes in the type of hydration products and results in high alkalinity (pore solution pH > 13.2). The addition of  $SO_4^{2-}$  did not promote the formation of AFt in CSA hydration but rather reduced the crystalline content in CSA-OPC paste and increased the amount of gel-like product, thereby impeding the hydration of  $C_4A_3\bar{S}$  and diminishing ettringite production.

(3) Magnesium ions ( $Mg^{2+}$ ) generally facilitate the hydration of CSA-OPC. Higher concentrations correspond to reduced porosity and increased strength. The inclusion of  $Mg^{2+}$  fosters the generation of ettringite and magnesium–aluminum phases, leading to elongated and thick ettringite crystals, and the cementitious material filling the voids within the skeleton increases. Moreover, an excessive concentration of  $Mg^{2+}$  can promote decalcification reactions, leading to the formation of brucite by reacting with the hydration products of CH, thereby enhancing the strength of the specimens.

**Author Contributions:** Formal analysis, C.W.; Funding acquisition, C.W.; Methodology, C.W.; Resources, C.W.; Validation, C.W.; Data curation, S.Z.; Project administration, S.Z.; Validation, S.Z.; Writing—original draft, S.Z.; Methodology, Q.O.; Project administration, Q.O.; Writing—review



& editing, Q.O.; Data curation, Y.Z.; Methodology, Y.Z. All authors have read and agreed to the published version of the manuscript.

**Funding:** This research was funded by Department of Science and Technology of Guangdong Province, grant number [2023A1515012727]; Department of Education of Guangdong Province: grant number [2021KQNCX021].

**Data Availability Statement:** The original contributions presented in the study are included in the article, further inquiries can be directed to the corresponding author.

**Conflicts of Interest:** The authors declare no conflict of interest.

## References

1. Miller, S.A.; Horvath, A.; Monteiro, P.J.M. Impacts of booming concrete production on water resources worldwide. *Nat. Sustain.* **2018**, *1*, 69–76. [[CrossRef](#)]
2. Telesca, A.; Marroccoli, M.; Coppola, L.; Coffetti, D.; Candamano, S. Tartaric acid effects on hydration development and physico-mechanical properties of blended calcium sulphoaluminate cements. *Cem. Concr. Compos.* **2021**, *124*, 104275. [[CrossRef](#)]
3. Sanfelix, S.G.; Zea-Garcia, J.D.; Londono-Zuluaga, D.; Santacruz, I.; De la Torre, A.G.; Kjoniksen, A.-L. Hydration development and thermal performance of calcium sulphoaluminate cements containing microencapsulated phase change materials. *Cem. Concr. Res.* **2020**, *132*, 106039. [[CrossRef](#)]
4. Ke, G.J.; Zhang, J.; Liu, Y.Z. Shrinkage characteristics of calcium sulphoaluminate cement concrete. *Constr. Build. Mater.* **2022**, *337*, 127627. [[CrossRef](#)]
5. Li, J.; Yan, J.; Xue, G.; Niu, J. Acoustic emission behavior of polyvinyl alcohol (PVA) fiber reinforced calcium sulphoaluminate cement mortar under flexural load. *J. Build. Eng.* **2021**, *40*, 102734. [[CrossRef](#)]
6. Hou, W.; Liu, Z.; He, F.; Huang, J.; Zhou, J. Sulfate diffusion in calcium sulphoaluminate mortar. *Constr. Build. Mater.* **2019**, *234*, 117312. [[CrossRef](#)]
7. Etxeberria, M.; Gonzalez-corominas, A.; Pardo, P. Influence of seawater and blast furnace cement employment on recycled aggregate concrete properties. *Constr. Build. Mater.* **2016**, *115*, 496–505. [[CrossRef](#)]
8. Qu, F.; Li, W.; Wang, K.; Tam, V.W.Y.; Zhang, S. Effects of seawater and undesalted sea sand on the hydration products, mechanical properties and microstructures of cement mortar. *Constr. Build. Mater.* **2021**, *310*, 125229. [[CrossRef](#)]
9. Zhang, Y.; Sun, Y.; Shen, P.; Lu, J.; Cai, Y.; Poon, C.S. Physicochemical investigation of Portland cement pastes prepared and cured with seawater. *Mater. Struct.* **2022**, *55*, 150. [[CrossRef](#)]
10. De Weerd, K.; Justnes, H. The effect of sea water on the phase assemblage of hydrated cement paste. *Cem. Concr. Compos.* **2015**, *55*, 215–222. [[CrossRef](#)]
11. Stroh, J.; Meng, B.; Emmerling, F. Deterioration of hardened cement paste under combined sulphate-chloride attack investigated by synchrotron XRD. *Solid State Sci.* **2016**, *56*, 29–44. [[CrossRef](#)]
12. Wang, C.; Liu, Z.; Zhang, T.; Zhang, Y.; Liu, Z.; Zhao, X. Influence of the Concentration of Seawater on the Early Hydration Properties of Calcium Sulphoaluminate (CSA) Cement: A Preliminary Study. *Buildings* **2021**, *11*, 243. [[CrossRef](#)]
13. Ragoug, R.; Metalssi, O.O.; Barberon, F.; Torrenti, J.M.; Roussel, N.; Divet, L.; De Lacaillerie, J.B.D. Durability of cement pastes exposed to external sulfate attack and leaching: Physical and chemical aspects. *Cem. Concr. Res.* **2019**, *116*, 134–145. [[CrossRef](#)]
14. Yuan, Q.; Shi, C.; De Schutter, G.; Audenaert, K.; Deng, D. Chloride binding of cement-based materials subjected to external chloride environment—A review. *Constr. Build. Mater.* **2009**, *23*, 1–13. [[CrossRef](#)]
15. Ben-Yair, M. The effect of chlorides on concrete in hot and arid regions. *Cem. Concr. Res.* **1974**, *4*, 405–416. [[CrossRef](#)]
16. Suryavanshi, A.K.; Narayan Swamy, R. Stability of Friedel's salt in carbonated concrete structural elements. *Cem. Concr. Res.* **1996**, *26*, 729–741. [[CrossRef](#)]
17. Kim, T.; Kang, C.; Hong, S.; Seo, K.Y. Investigating the Effects of Polyaluminum Chloride on the Properties of Ordinary Portland Cement. *Materials* **2019**, *12*, 3290. [[CrossRef](#)]
18. Cheng, Y.; Li, Z.; Huang, X.; Bai, X. Effect of Friedel's salt on strength enhancement of stabilized chloride saline soil. *J. Cent. South Univ.* **2017**, *24*, 937–946. [[CrossRef](#)]
19. Cheng, S.; Shui, Z.; Sun, T.; Gao, X.; Guo, C. Effects of sulfate and magnesium ion on the chloride transportation behavior and binding capacity of Portland cement mortar. *Constr. Build. Mater.* **2019**, *204*, 265–275. [[CrossRef](#)]
20. Ding, Q.; Yang, J.; Zhang, G.; Hou, D. Effect of magnesium on the C-S-H nanostructure evolution and aluminate phases transition in cement-slag blend. *J. Wuhan Univ. Technol.-Mater. Sci. Ed.* **2018**, *33*, 108–116. [[CrossRef](#)]
21. Bonen, D.; Cohen, M.D. Magnesium sulfate attack on portland cement paste-I. *Microstructural analysis.* *Cem. Concr. Res.* **1992**, *22*, 169–180. [[CrossRef](#)]
22. Li, X.; Shui, Z.; Yu, R.; Wang, X. Magnesium induced hydration kinetics of ultra-high performance concrete (UHPC) served in marine environment: Experiments and modelling. *Constr. Build. Mater.* **2019**, *224*, 1056–1068. [[CrossRef](#)]
23. Xiao, J.; Qiang, C.; Nanni, A.; Zhang, K. Use of sea-sand and seawater in concrete construction: Current status and future opportunities. *Constr. Build. Mater.* **2017**, *155*, 1101–1111. [[CrossRef](#)]



24. Zhang, J.; Chang, J.; Zhang, P.; Wang, T. Effects of C<sub>2</sub>H<sub>2</sub> and CH on Strength and Hydration of Calcium Sulphoaluminate Cement Prepared from Phosphogypsum. *Buildings* **2022**, *12*, 1692. [[CrossRef](#)]
25. Cao, Y.; Guo, L.; Chen, B.; Wu, J. Thermodynamic modelling and experimental investigation on chloride binding in cement exposed to chloride and chloride-sulfate solution. *Constr. Build. Mater.* **2020**, *246*, 118398. [[CrossRef](#)]
26. Zhang, Y.; Zhao, Q.; Gao, Z.; Chang, J. Microstructure Control of AH<sub>3</sub> Gel Formed in Various Calcium Sulfoaluminate Cements as a Function of pH. *ACS Sustain. Chem. Eng.* **2021**, *9*, 11534–11547. [[CrossRef](#)]
27. Khalil, N.; Aouad, G.; Kleib, J.; Rémond, S. Portland/Sulfoaluminate Cement Blends for the Control of Early Age Hydration and Yield Stress. *Buildings* **2023**, *13*, 409. [[CrossRef](#)]
28. GB/T 17671-1999; Method of Testing Cements—Determination of Strength. State Bureau of Quality and Technical Supervision: Beijing, China, 1999.
29. ASTM C20-2000; Standard Test Methods for Apparent Porosity, Water Absorption, Apparent Specific Gravity, and Bulk Density of Burned Refractor Brick and Shapes by Boiling Water. ASTM: West Conshohocken, PA, USA, 2015.
30. Deng, X.; Guo, H.; Tan, H.; Zhang, J.; Zheng, Z.; Li, M.; Chen, P.; He, X.; Yang, J.; Wang, J. Comparison on early hydration of Portland cement and sulfoaluminate cement in the presence of nano ettringite. *Constr. Build. Mater.* **2022**, *360*, 129516. [[CrossRef](#)]
31. Lu, Y.; Shi, G.; Liu, Y.; Ding, Z.; Pan, J.; Qin, D.; Dong, B.; Shao, H. Study on the effect of chloride ion on the early age hydration process of concrete by a non-contact monitoring method. *Constr. Build. Mater.* **2018**, *172*, 499–508. [[CrossRef](#)]
32. Burlion, N.; Bernard, D.; Chen, D. X-ray microtomography: Application to microstructure analysis of a cementitious material during leaching process. *Cem. Concr. Res.* **2006**, *36*, 346–357. [[CrossRef](#)]
33. Tosun, K.; Baradan, B. Effect of ettringite morphology on DEF-related expansion. *Cem. Concr. Compos.* **2010**, *32*, 271–280. [[CrossRef](#)]
34. Diamond, S.; Landis, E. Microstructural features of a mortar as seen by computed microtomography. *Mater. Struct.* **2006**, *40*, 989–993. [[CrossRef](#)]
35. Odler, I.; Colán-Subauste, J. Investigations on cement expansion associated with ettringite formation. *Cem. Concr. Res.* **1999**, *29*, 731–735. [[CrossRef](#)]
36. Thiebaut, Y.; Multon, S.; Sellier, A.; Lacarrière, L.; Boutillon, L.; Belili, D.; Linger, L.; Cussigh, F.; Hadji, S. Effects of stress on concrete expansion due to delayed ettringite formation. *Constr. Build. Mater.* **2018**, *183*, 626–641. [[CrossRef](#)]
37. Bertola, F.; Gastaldi, D.; Irico, S.; Paul, G.; Canonico, F. Influence of the amount of calcium sulfate on physical/mineralogical properties and carbonation resistance of CSA-based cements. *Cem. Concr. Res.* **2020**, *151*, 106634. [[CrossRef](#)]
38. Liao, Y.; Yao, J.; Deng, F.; Li, H.; Wang, K.; Tang, S. Hydration behavior and strength development of supersulfated cement prepared by calcined phosphogypsum and slaked lime. *J. Build. Eng.* **2023**, *80*, 2352–7102. [[CrossRef](#)]
39. Padilla-Encinas, P.; Palomo, A.; Blanco-Varela, M.T.; Fernandez-Jimenez, A. Calcium sulfoaluminate clinker hydration at different alkali concentrations. *Cem. Concr. Res.* **2020**, *138*, 106251. [[CrossRef](#)]
40. Guo, H.; Liu, Y.; Tai, B.; Zhang, Z.; Zhu, Y. Effect of environmental pH value on mechanical properties and microstructure of hardened sulfoaluminate cement paste. *Constr. Build. Mater.* **2020**, *325*, 126848. [[CrossRef](#)]
41. Ben Haha, M.; Winnefeld, F.; Pisch, A. Advances in understanding ye'elimite-rich cements. *Cem. Concr. Res.* **2019**, *12*, 105778. [[CrossRef](#)]
42. Sánchez-Herrero, M.J.; Fernández-Jiménez, A.; Palomo, A. C<sub>4</sub>A<sub>3</sub>S̄ hydration in different alkaline media. *Cem. Concr. Res.* **2013**, *46*, 41–49. [[CrossRef](#)]
43. Sánchez-Herrero, M.J.; Fernández-Jiménez, A.; Palomo, A. C<sub>3</sub>S and C<sub>2</sub>S hydration in the presence of Na<sub>2</sub>CO<sub>3</sub> and Na<sub>2</sub>SO<sub>4</sub>. *J. Am. Ceram. Soc.* **2017**, *100*, 3188–3198. [[CrossRef](#)]
44. Sánchez-Herrero, M.J.; Fernández-Jiménez, A.; Palomo, A. Alkaline Hydration Of C<sub>2</sub>S and C<sub>3</sub>S. *J. Am. Ceram. Soc.* **2016**, *99*, 604–611. [[CrossRef](#)]
45. Liao, Y.; Wang, S.; Wang, S.; Siraj Al Qunaynah Wan, S.; Yuan, Z.; Xu, P.; Tang, S. A study on the hydration of calcium aluminate cement pastes containing silica fume using non-contact electrical resistivity measurement. *J. Mater. Res. Technol.* **2023**, *24*, 8135–8149. [[CrossRef](#)]
46. Wang, L.; Jin, M.; Zhou, S.; Tang, S.; Lu, X. Investigation of microstructure of C-S-H and micro-mechanics of cement pastes under NH<sub>4</sub>NO<sub>3</sub> dissolution by <sup>29</sup>Si MAS NMR and microhardness. *Measurement* **2021**, *185*, 110019. [[CrossRef](#)]
47. Wang, L.; Jin, M.; Wu, Y.; Zhou, Y.; Tang, S. Hydration, shrinkage, pore structure and fractal dimension of silica fume modified low heat Portland cement-based materials. *Constr. Build. Mater.* **2021**, *272*, 121952. [[CrossRef](#)]

**Disclaimer/Publisher's Note:** The statements, opinions and data contained in all publications are solely those of the individual author(s) and contributor(s) and not of MDPI and/or the editor(s). MDPI and/or the editor(s) disclaim responsibility for any injury to people or property resulting from any ideas, methods, instructions or products referred to in the content.